Impact of Pore Connectivity on Quantification of

Mineral Accessibility in Sandstone Samples

- 3 Md. Fahim Salek, Fangi Qin, Parisa Asadi, Chidera Iloejesi, Olivia Brunhoeber, Mukseet
- 4 Mahmood, Lauren E. Beckingham*
- 5 Department of Civil and Environmental Engineering, Auburn University
- 6 Auburn, Al 36830, USA
- 7 *leb@auburn.edu
- 8 Abstract

18

1

2

9 Characterization of microscale features and mineral distributions in rock samples can be facilitated 10 non-destructively with imaging analysis. Scanning electron microscopy (SEM) with backscatter 11 electron (BSE) and energy dispersive spectroscopy (EDS) is particularly valuable and can be 12 utilized to identify minerals. Mineral segmentation coupled with quantitative image processing 13 can yield mineral volume fractions and accessibility from these images. Prior estimates of mineral 14 accessibility from images have improved simulations of mineral reaction rates but it is unclear 15 how pore connectivity should be accounted for. This is further complex in samples with clay 16 minerals where nanopores in clays need to be considered. Here, impacts of different approaches 17 to assess pore connectivity on quantification of mineral accessibility are considered for seven

sandstone samples with varying composition. Mineral accessibilities are calculated by counting

interfacial pixels between associated minerals and adjacent pores from the 2D mineral segmented maps. Three types of accessibility are considered: the first approach accounts for all the macropore space, the second approach considers only the 2D connected macropores, and the third approach includes 2D connected porosity considering nanopores in clays. Observed variations in accessibility for most mineral phases are within one order of magnitude when nanopore connectivity is considered and thus not anticipated to largely impact the simulated reactivity of samples. However, greater variations were observed for clay minerals which may impact long-term simulations (years). Larger variations in accessibility were also noted for carbonate minerals but only some samples contained carbonate phases and additional data is needed to assess the trends.

- 29 Keywords: Mineral Accessibility, Mineral Segmentation, Nanopore connectivity, Scanning
- 30 Electron Microscopy, Effective Porosity

1. Introduction

19

20

21

22

23

24

25

26

27

28

- 32 Understanding mineral reactions and reaction rates in porous media are critical to assessing and
- predicting transport in reactive environmental systems, including natural weathering processes ^{1–}
- 34 ³, contaminant transport ⁴⁻⁸, CO₂ injection for storage ^{9,10} or enhanced oil recovery ^{11–14}, and
- 35 compressed energy storage ^{15,16}. In these and other systems, mineral dissolution occurs due to
- 36 perturbations from equilibrium.
- 37 Mineral dissolution rates are typically determined using batch experiments with single mineral
- 38 phases, but there is a noted discrepancy in the rate of reaction observed in the laboratory in
- 39 comparison with field observed reaction rates ^{2,17–20}. In part, this is due to porous media effects
- 40 and a misestimation of mineral reactive surface area in porous media ^{21–23}. Advanced imaging of

natural porous media has revealed that mineral surfaces may be occluded by clay mineral coatings or limited by pore connectivity such that those surfaces are not accessible for reaction ^{22,24–26}. Mineral accessible surface areas, those that will be in contact with reactive fluids, have been noted to improve simulation of mineral reaction rates in multi-mineralic porous media as compared to other more traditional means of reactive surface area estimation ²². Combining surface roughness scaling factors can even improve the accessible surface area estimation to the atomic level ²⁷. As such, mineral accessibility may better reflect the proportion of mineral phases available for reaction in porous media as compared to mineral volume or weight fractions. Mineral accessibilities can be quantified using imaging analysis ^{24,26}. Mineral maps can be created by processing 2D Scanning Electron Microscopy (SEM) images where individual mineral phases are identified by combining backscattered electron (BSE) and energy-dispersive x-ray spectroscopy (EDS) images ^{22,24,26}. Properties of the sample including porosity, mineral volume fractions (abundances), and mineral accessibilities are then determined from the mineral map by pixel counting ^{22,25,26}. Mineral accessibility is quantified by computing the number of mineral pixels of each phase at the pore-mineral interface. In the simplest approximation, this assumes reactive fluids may be present in all pore spaces. However, pore connectivity may limit fluid flow and result in some regions that are inaccessible to fluid flow. This has been accounted for by evaluating pore connectivity using a burning algorithm to map connected pores in the 2D mineral map and deeming only those minerals adjacent to the identified connected pore pixels as accessible ^{22,26}. 2D SEM imaging cannot capture nanopore connectivity, but high-resolution Focused Ion Beam SEM (FIB-SEM) imaging of clay minerals has revealed clay minerals have abundant, well-connected nano porosity ^{22,26}. As such, nanopores in clays may not limit but instead, contribute to overall pore

41

42

43

44

45

46

47

48

49

50

51

52

53

54

55

56

57

58

59

60

61

62

connectivity and alter the relative proportion of mineral's availability ^{22,26}. However, this approach still only reflects connectivity in 2D such that assuming all pores are connected may better reflect actual pore connectivity of sandstone samples. While pore connectivity can be readily determined in 3D from 3D X-ray computed tomography (X-ray CT) images, mineral phases, and thus mineral accessibility, cannot. Additional resolution limitations may underestimate overall 3D connectivity estimates. As such, mineral accessibilities can only be quantified in 2D images, but it is unknown to what extent estimated mineral accessibility would change given variations in estimated pore connectivity.

The objective of this work is to enhance understanding of mineral accessibility in sandstone samples and variations in image quantified mineral accessibilities due to different pore connectivity approaches. Here, the impact of accounting for pore connectivity on mineral accessibility is considered for seven sandstone samples of varying compositions. Pore connectivity and mineral accessibility are determined, excluding, and including nanopore connectivity, and results compared to discern the impact of pore connectivity estimates on the quantification of mineral accessibility.

2. Materials and Methods

2.1 Samples

Seven sandstone samples with varying clay content were selected for analysis in this work. This includes samples from the Bandera Grey, Bandera Brown, Bentheimer, Kentucky, and Torrey Buff formations obtained from Kocurek Industries. Two additional samples from the Lower Tuscaloosa and Paluxy formations were obtained from the Geological Survey of Alabama. From X-ray Diffraction (XRD) analysis provided by Kocurek Industries and prior evaluation of similar

- 86 samples in the literature ^{28,29}, these samples are predominantly quartz (59%-94%) with additional
- 87 feldspar, carbonate, and clay minerals (Table 1).
- 88 **Table 1**: Mineral abundances (wt%) from XRD analysis as obtained from Kocurek Industries¹,
- 89 Soong et al. $(2016)^2$ and Guan $(2012)^3$

Sample\Mineral	Quartz	Albite	K- Feldspar	Calcite	Dolomite	Kaolinite	Illite	Chlorite	Smectite	Siderite
Bandera Grey ¹	59	12	0	0	15	3	10	1	0	0
Bandera Brown ¹	66	13	2	3	0	7	11	2	0	0
Bentheimer ¹	94.4	1.2	1.2	0.5	0	0	0	0	0	0
Kentucky ¹	66	17	3	0	0	trace	14	0	0	0
Torrey Buff ¹	48	0	6	0	24	16	7	0	0	0
Lower Tuscaloosa ²	92	0	3	0	1	1	1	2	0	0
Paluxy ³	66	1	3	0	0	13	7	1	0	6

- Polished thick sections (0.5 cm thickness) (Kocurek Industries samples) and polished thin
- 91 sections (Geological Survey of Alabama samples) were created by Applied Petrographic Services,
- 92 Inc. (Westmoreland, Pennsylvania) for SEM imaging analysis. To prepare for SEM imaging, a
- 93 conductive carbon coating was applied to each thin section using EMS 550× Sputter Coating
- 94 Device at Auburn University. Thick sections were left uncoated.

95

2.2 Image acquisition and mineral properties quantification

- Mineral properties including porosity, mineral abundance, and mineral accessibility were quantified from 2D SEM BSE and EDS images. SEM BSE images of the seven samples were
- 98 captured using a ZEISS EVO 50VP Scanning Electron Microscope at Auburn University. Carbon—
- 99 coated thin sections were imaged under high vacuum mode while the uncoated thick sections were

imaged under variable pressure mode. The resolution and size of each image are given in supplementary information (Table S1). A representative elementary volume (REV) analysis was carried out on collected images for each sample to ensure each image area was sufficient. SEM BSE images were first manually thresholded in ImageJ to separate grain and pore pixels. Several sub-areas of increasing size were selected from the segmented image and the porosity was computed by pixel counting.

EDS elemental maps were also obtained for each sample to help identify mineral phases. Images were registered in ImageJ and additional processing and mineral segmentation of the images followed the approach used in Landrot et al. (2012) and Beckingham et al. (2016)^{26,30}. Briefly, SEM-EDS elemental maps were enhanced with filters in ImageJ and customized noise reduction Matlab codes. Minerals were then identified based on elemental maps and SEM BSE grayscale intensity. Each pixel was assigned to a specific mineral and expressed as a unique color, creating a processed mineral map. This part of the processing was performed in Matlab (original code modified for each image) and ImageJ.

Following image segmentation, mineral abundances were calculated by counting mineral pixels with the same color while mineral accessibilities were calculated by counting mineral pixels adjacent to pore pixels. Mineral abundance refers to the volume fraction of each mineral phase, and mineral accessibility refers to the percentage of each mineral's surface that is adjacent to the pores. To determine accessibilities, pore-mineral interfacial pixels were first identified using codes written in Matlab. The accessibility of each mineral phase was then calculated from the number of interfacial pixels of each mineral phase divided by the total number of interfacial pixels.

Here, three different means of calculating mineral accessibility were considered. This included defining interfacial pixels as mineral pixels adjacent to 1) pores identified in the processed mineral

map, which will be referred to as macropores, 2) connected macropores identified in the processed mineral map, and 3) connected nano and macropores in processed mineral maps. In cases that considered connected pores, these pore pixels were identified by using a burning algorithm after Landrot et al. (2012)²⁶. The algorithm first identifies pore pixels at the image edges then searches inward for adjacent (connected) pore pixels, continuing inwards until it completes searching in all four directions²⁶. Identified connected macropores are displayed in white and connected nanopores in clays presented in three different colors for the three different clays. Connected porosity was calculated as the total number of connected pore pixels divided by the total pixels of the image. In the third estimation, we assume all clay minerals have abundant, well-connected nanoporosity as observed in prior Focused Ion Beam (FIB) SEM imaging analysis of clay minerals^{26,30}.

3 Results

3.1 Image processing and mineral property quantification

SEM BSE images, mineral phase segmented maps, and 2D pore connectivity images were produced for each sample. Mineral abundance obtained from the 2D segmented map is presented in Table 2. As expected from the prior mineral abundance data, quartz, feldspars, carbonates, and clay, as well as some additional minerals like siderite, zircon, mica (muscovite and biotite), and some oxides (ilmenite, anatase, and magnetite) were identified in the samples.

Table 2: Mineral abundances (vol%) and accessibilities (%) determined from the 2D mineral segmented maps using three approaches.

	Minerals	Abundance (vol%)		Accessibility	Accessibility
			Accessibility	(Only	(Connected
Sample			(All Macro	Connected	Macro &
			Pores)	Macro	Nano
				Pores)	Pores)
Bandera Grey	Quartz	63.46	57.98	70.82	62.63

	K-feldspar	12.12	7.32	6.12	5.53
	Albite	10.22	8.81	7.28	7.45
	Calcite	5.69	1.15	1	0.84
	Illite	6.39	23.34	14.78	23.45
	muscovite	0.68	0.45	0	0
	Titanium Oxide	0.28	0.23	0	0.09
	Biotite	1.14	0.7	0	0
	Quartz	73.48	62.58	69.42	54.81
	K-feldspar	8.33	5.47	2.57	5.48
	Albite	10.24	5.57	4.2	6.02
	Calcite	0.007	0.01	0	0
Bandera Brown	Kaolinite	4.31	16.05	12.86	21.83
	Illite	1.17	4.31	2.7	6.35
	Chlorite	0.48	2.33	4.5	3.45
	Titanium Oxide	0.47	0.14	0.11	0.08
	Iron Oxide	1.49	3.53	3.63	1.97
	Quartz	95.32	83.65	84.79	80.05
	K-feldspar	2.71	2.72	2.35	2.99
Bentheimer	Calcite	0.0003	0	0	0
	Kaolinite	1.64	13.24	12.6	16.71
	Ilmenite	0.4	0.39	0.25	0.24
	Quartz	62.58	47.49	33.25	34.29
	K-feldspar	2.95	2.2	0.27	4.97
	Albite	16.79	10.67	14.05	10.37
	Zircon	0.37	0.06	0	0.34
Kentucky	Ilmenite	0.29	0.11	0.5	0.99
•	Illite	11.73	35.51	49.68	31.25
	Muscovite	2.55	2.51	0.37	4.79
	Titanium Oxide	0.17	0.1	0.05	0.71
	Iron Oxide	2.6	1.35	1.83	12.27
Torrey Buff	Quartz	56.73	53.38	57.74	51.68
	K-feldspar	5.83	2.87	1.82	3.74
	Iron-rich				
	dolomite	12.04	2.78	1.53	1.65
	Dolomite	13.28	3.71	1.38	1
	Kaolinite	10.62	34.36	35.04	39.25
	Illite	0.59	2.62	2.17	2.62
	Zircon	0.19	0.015	0.006	0.003
	Titanium Oxide	0.34	0.05	0.11	0.05
	Iron Oxide	0.37	0.22	0.18	0
	Quartz	92.03	79.32	83.33	79.48
Lower	K-feldspar	1.58	3.32	1.47	2.4
Tuscaloosa	Albite	0.49	0.58	0.39	0.3

	Dolomite	1.48	1.67	1.17	2.13
	Kaolinite	3.67	14.82	13.41	15.51
	Muscovite	0.53	0.28	0.22	0.18
Paluxy	Quartz	69.31	51.35	51.96	47.24
	K-feldspar	1.21	1.56	1.04	1.05
	Albite	24.5	25.86	20.02	17.86
	Calcite	0.78	0.46	0.14	0.96
	Kaolinite	2.26	16.9	24.35	28.12
	Illite	0.24	2.04	1.38	3.24
	Siderite	0.29	0.48	0.37	0.35
	Titanium Oxide	0.81	0.39	0.14	0.24
	Muscovite	0.6	0.97	0.6	0.95

As discussed in section 2.2, mineral accessibilities were quantified for every mineral in each sample. The accessibility data is presented in Table 2. These values indicate the proportion of each mineral at the pore-grain interface. It is of interest to consider the interfaces of the grains that will be in contact with the potential reactive fluid. If the pore space is well connected, reactive fluid may be in all identified pores. However, limitations in pore connectivity can occur and restrict which mineral surfaces are accessible to the reactive fluid. Both scenarios are considered here in calculations of mineral accessibility. Pore connectivity is identified using a burning algorithm where connected porosity is first identified only considering macropores and then considering connectivity through clay nanopores. Connected macropores are shown in white in Figures 1-7 (d), while three different colors are used to present the nanopore connectivity in clays in Figures 1-7 (e): kaolinite in turquoise, chlorite in cyan, and illite in teal.

3.1.1 Bandera Grey

The SEM BSE and mineral phase segmented map of the Bandera Grey sandstone sample is shown in Figure 1 (a and b). It is predominately comprised of quartz and two feldspar minerals, K-feldspar and albite. The calculated porosity from the BSE image is 15%. Accessibility is calculated for all the minerals considering the three approaches. Figure 1c shows the mineral

segmented map where all the macropores are assumed to be filled with reactive fluid and represented in white color. Similar to the highest abundance, quartz has the highest accessibility. The accessibility of the clay phase, smectite/illite is four times higher than the abundance of clay minerals.

When considering macropore connectivity, the sample has very low pore connectivity, which is reflected in Figure 1d. The corresponding effective porosity is 1.66%. Considering connected macropores, quartz has the highest accessibility among all the mineral phases, followed by smectite/illite. The accessibility of K-feldspar and albite reduce when considering connected macropores to 6.12% and 7.28%, respectively. Mica minerals, muscovite and biotite, are not accessible due to low macropore connectivity. Accounting for multi-scale pore connectivity, including nanopore connectivity through smectite/illite, there is a minor increase in the effective porosity (from 1.66% to 2.21%). Quartz accessibility is the highest and agrees well with quartz abundance, whereas K-feldspar and albite have accessibilities approximately half of their abundances. Accessibility values increase significantly for smectite/illite in comparison with only considering macropore connectivity.

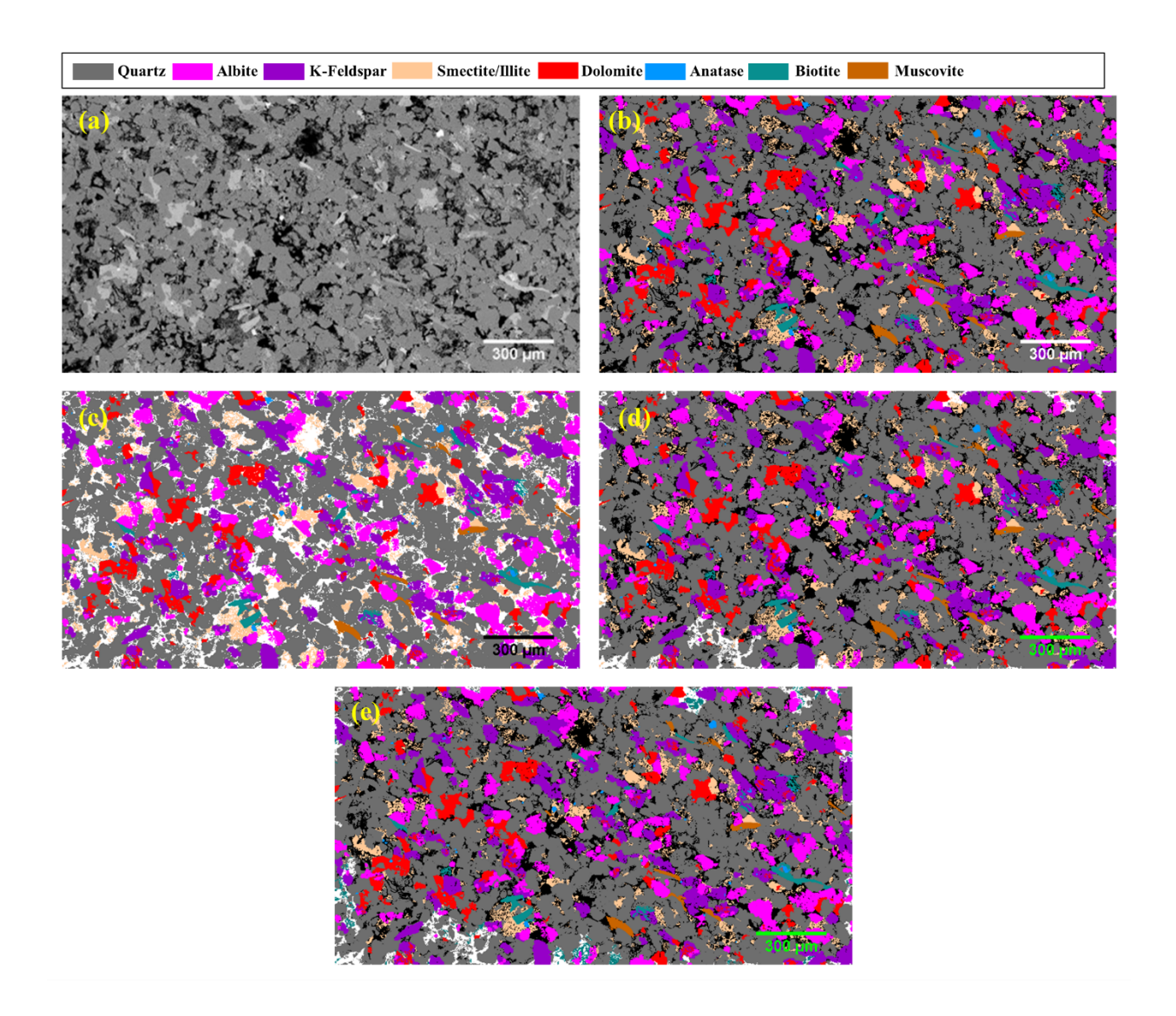


Figure 1: a) SEM BSE image of sample collected from Bandera Grey formation; b) mineral phase segmented map; c) mineral map considering all macro pores accessible; d) mineral map considering macro pore connectivity; e) mineral map including nano pore connectivity

3.1.2 Bandera Brown:

The SEM BSE image of the Bandera Brown sample and corresponding processed mineral map are in Figures 2 (a and b). A total of nine minerals are identified, with the majority of the sample comprised of quartz. There are three clay minerals – kaolinite, illite, and chlorite with a

total abundance of 5.96%. The porosity is calculated to be 21%. When all the macropores are considered, the accessibility of quartz is slightly less than the abundance while accessibilities are significantly less than abundances for K-feldspar and albite. On the other hand, the accessibility of clay minerals is about four times their abundance. Calcite accessibility is similar to its abundance.

Consideration of macropore pore connectivity significantly reduces the effective porosity to 5.2%. The accessibility of quartz remains high and close to the it's abundance. While K-feldspar and albite have higher abundances than clay minerals (kaolinite, illite, and chlorite) the accessibility of the clay minerals is higher. Calcite only has 0.007% abundance, and it is embedded in quartz grains, therefore, its accessibility is 0%. Figure 2e shows the mineral map considering nanopore connectivity in all three clays in the sample. Accounting for nanopore connectivity increases the effective porosity to 8.91%. Also, more albite and K-feldspar become accessible (see red boxes in Figure 2e). The accessibility of kaolinite also increases significantly from 12.86% to 21.83%.

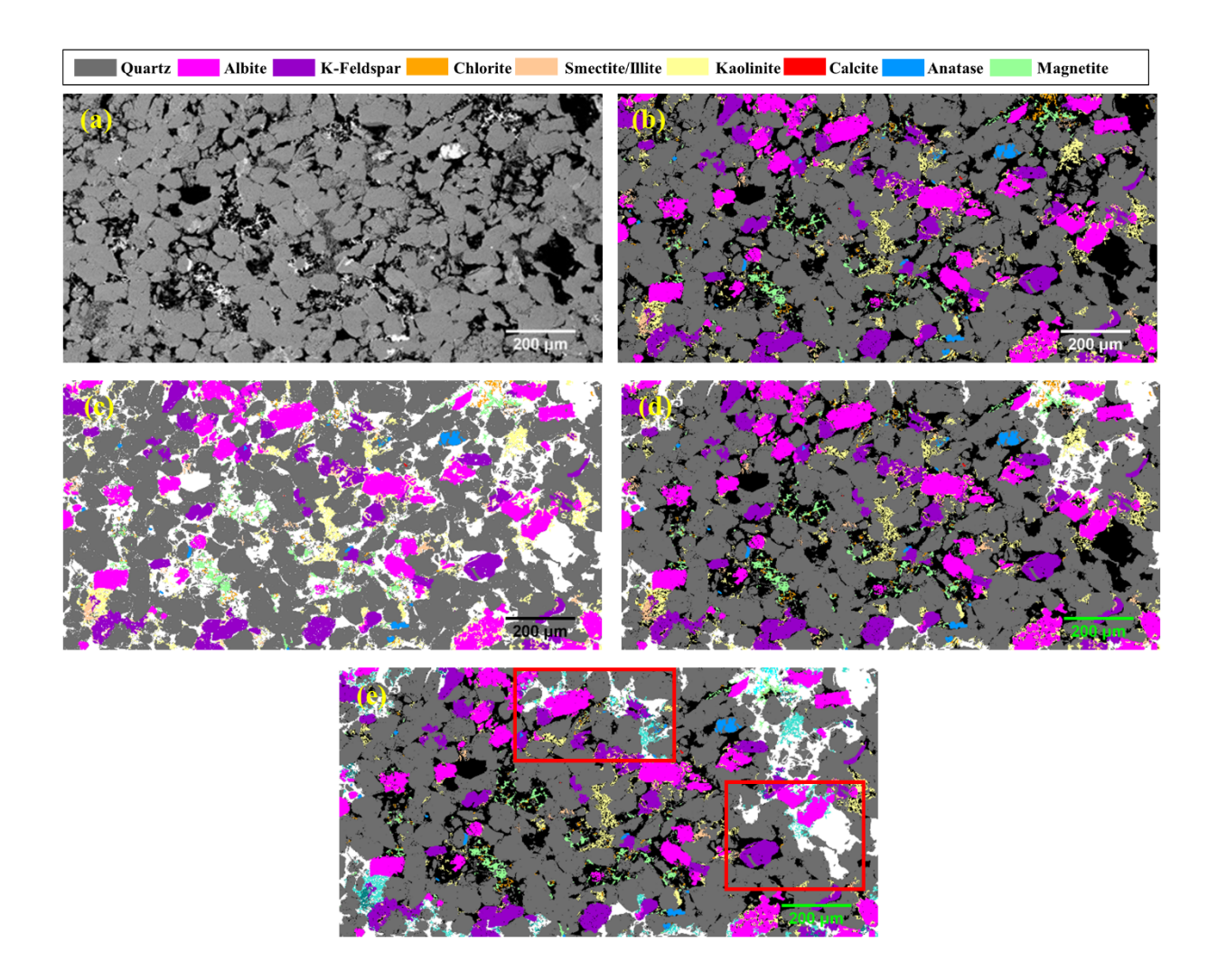


Figure 2: a) SEM BSE image of the sample collected from Bandera Brown formation; b) mineral phase segmented map c) mineral map considering all macropores accessible; d) mineral map considering macropore connectivity; e) mineral map including nanopore connectivity.

3.1.3 Bentheimer:

There are six mineral species identified in the BSE image of Bentheimer sample (Figure 3). Quartz has more than 95% abundance. This sample has a high porosity, 34.92%, measured from the 2D mineral map. When considering all macropores as accessible (Figure 3c), quartz has an accessibility of 83.65%, which is less than the abundance of quartz. The accessibility of K-feldspar

agrees well with its abundance, whereas calcite is inaccessible. The accessibility of kaolinite is 13.24%, significantly higher than its abundance.

Considering mineral interfaces accessible to connected macropores (Figure 3d), 84.79% are quartz, which is similar to when connectivity was not considered. About 12.6% of accessible surfaces are kaolinite, which is significantly higher than the relative abundance of kaolinite. Accounting nanopore connectivity (Figure 3e) decreases accessibility of quartz and increases accessibility of k-feldspar and kaolinite. Calcite is inaccessible in this case too. Effective porosities reduced to 15.68% and 18.45% considering connectivity in macro and nanoscales respectively.

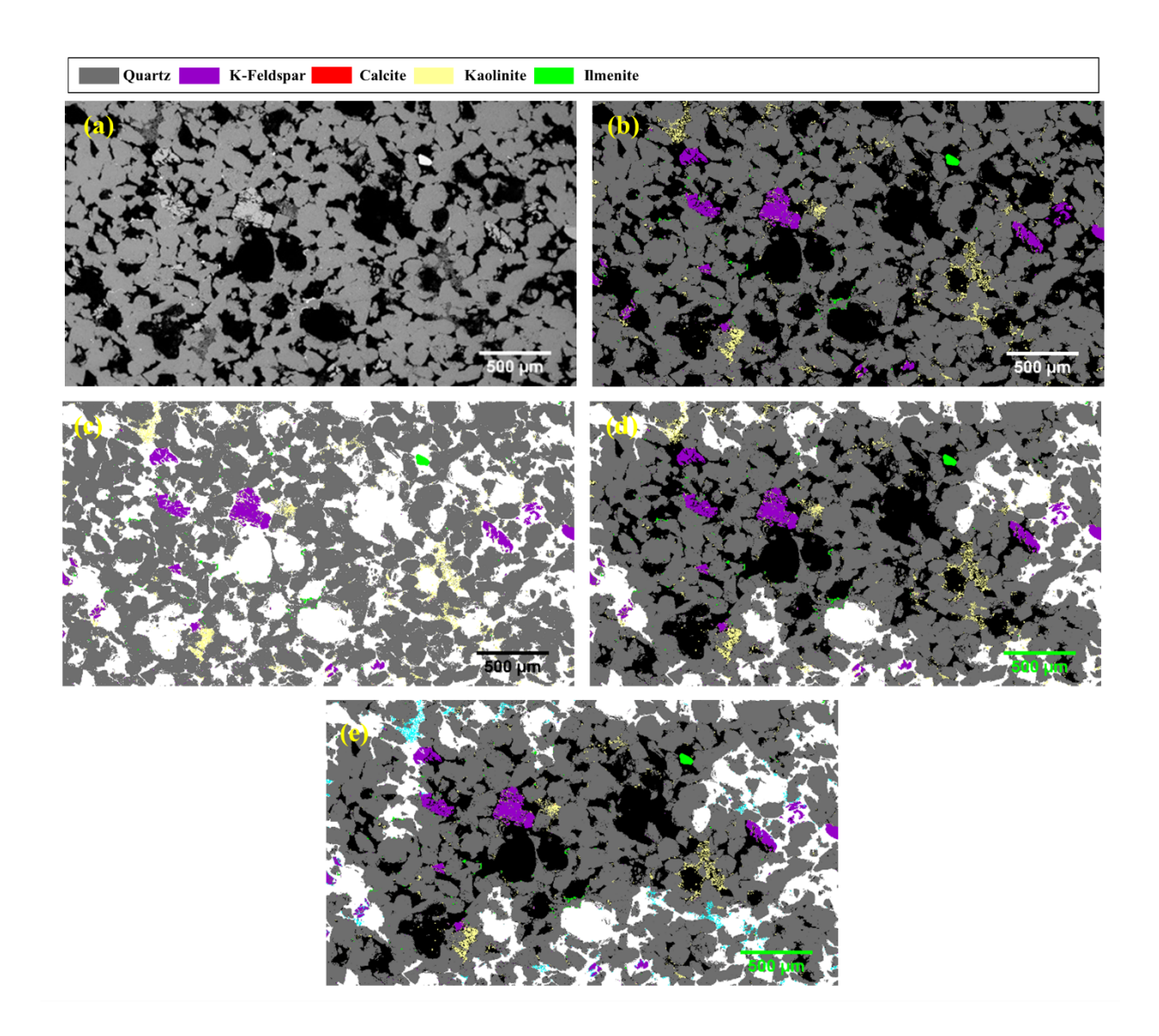


Figure 3: a) SEM BSE image of Bentheimer sandstone; b) mineral phase segmented map c) mineral map considering all macro pore accessible; d) mineral map considering macro pore connectivity; e) mineral map including nano pore connectivity

3.1.4 Kentucky:

The original and processed images for the Kentucky sandstone sample are shown in Figures 4 (a and b). Among the seven samples considered in this work, the Kentucky sandstone sample has the lowest porosity. The porosity calculated from the BSE image (Figure 4a) is 13.25%. Nine

mineral species are identified in the image and mapped in Figure 4b. Quartz is the most dominant phase with over 62% abundance, followed by albite and smectite/illite. Figure 4c shows the mineral segmented map when all the mineral surfaces are considered accessible. Quartz, which is the dominant phase, has an accessibility of 47.49%, which is significantly lower than its abundance. The accessibility of K-feldspar and muscovite agree well with their abundances while illite accessibility is more than three times its volume fraction. Having the lowest porosity, the sample is also very low on pore connectivity when only macropores are considered (effective porosity 1.25%). As for accessibility, smectite/illite has the highest accessibility, 49.68%, which is significantly higher than its abundance and its accessibility when connectivity is not considered. The accessibilities of quartz and albite are 33.25% and 14.05%, respectively, which is less than the abundance of quartz but similar to the abundance of albite. Zircon is not accessible to the connected pore space. Consideration of nanopore connectivity allows a lot of magnetite grains to be accessible (red boxes, Figure 4e) resulting in an increase in accessibility of 12.27% from 1.83%, while for albite and illite, the values decrease. The effective porosity increases to 4.27% when nanopore connectivity is included.

220

221

222

223

224

225

226

227

228

229

230

231

232

233

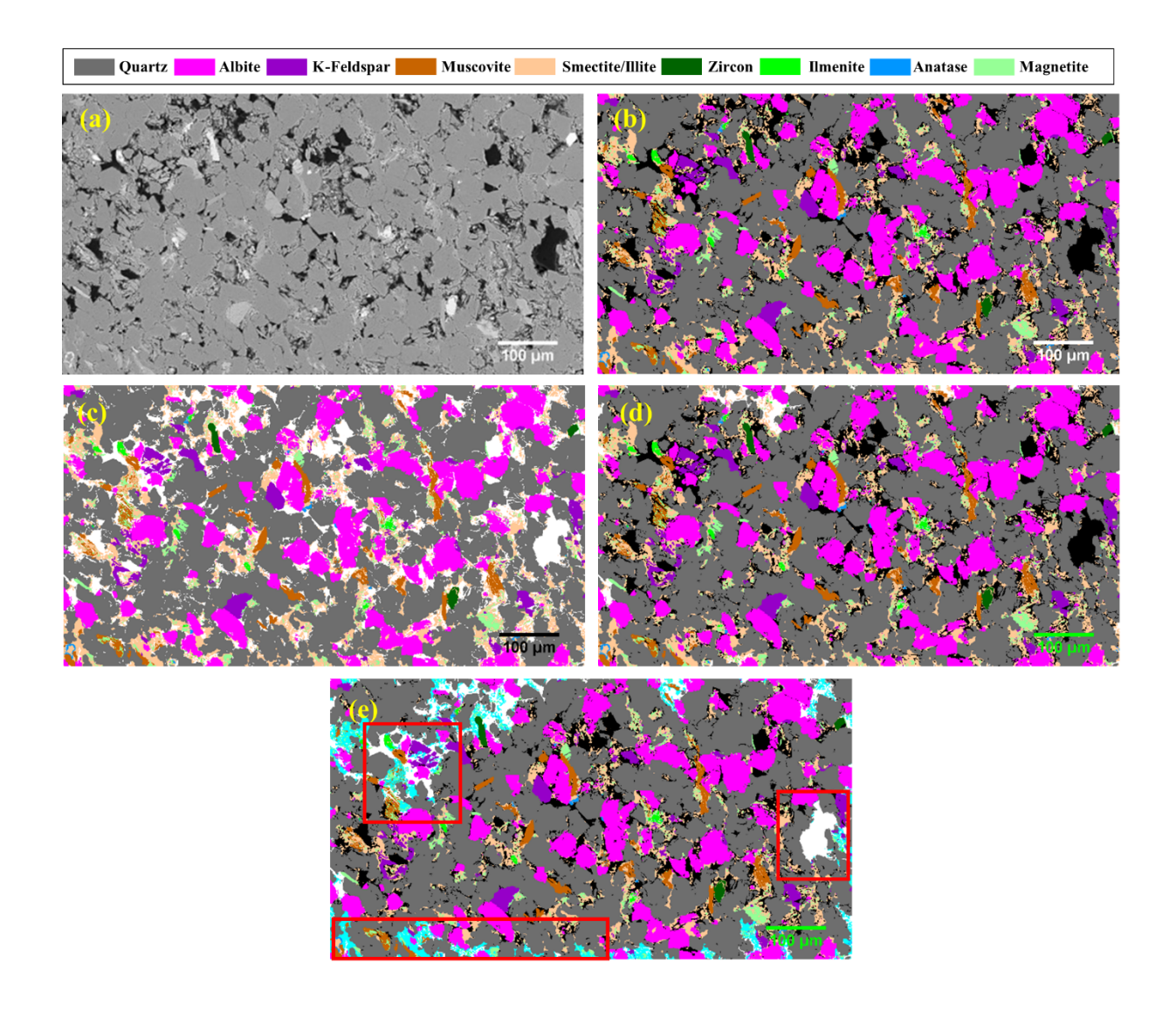


Figure 4: a) SEM BSE image of Kentucky sandstone; b) mineral phase segmented map; c) mineral map considering all macropore accessible; d) mineral map considering macropore connectivity; e) mineral map including nanopore connectivity

3.1.5 Torrey Buff

Figures 5 (a and b) show the original BSE SEM image and Torrey Buff sample's colored mineral segmented map, respectively. There are eight different minerals identified, and more than half of the total volume is comprised of quartz. Another major phase identified from the mineral map is dolomite, half of which is rich in iron. The sample has a high amount of clay. The calculated

porosity from the mineral segmented map is 20.3%. When accessibility is calculated considering all the macropores, quartz has a similar value for accessibility as abundance. K-feldspar and dolomite have accessibilities significantly lower than their abundance. Both of the clay minerals have high accessibility (34.36% and 2.62%) as compared to abundance.

When considering connected macropores, quartz has the highest accessibility, similar to its abundance, while kaolinite has significantly higher accessibility than abundance. As the sample has a higher amount of clay distributed throughout the sample (Figure 5b) considering nanopore connectivity (Figure 5e) significantly increases the effective porosity from 3.22% to 10.88%. The resulting accessibility of quartz decreases, while for K-feldspar, kaolinite, and illite, the values increase. The effective porosity also increases from 3.22% to 10.88% when nanopore connectivity is included.

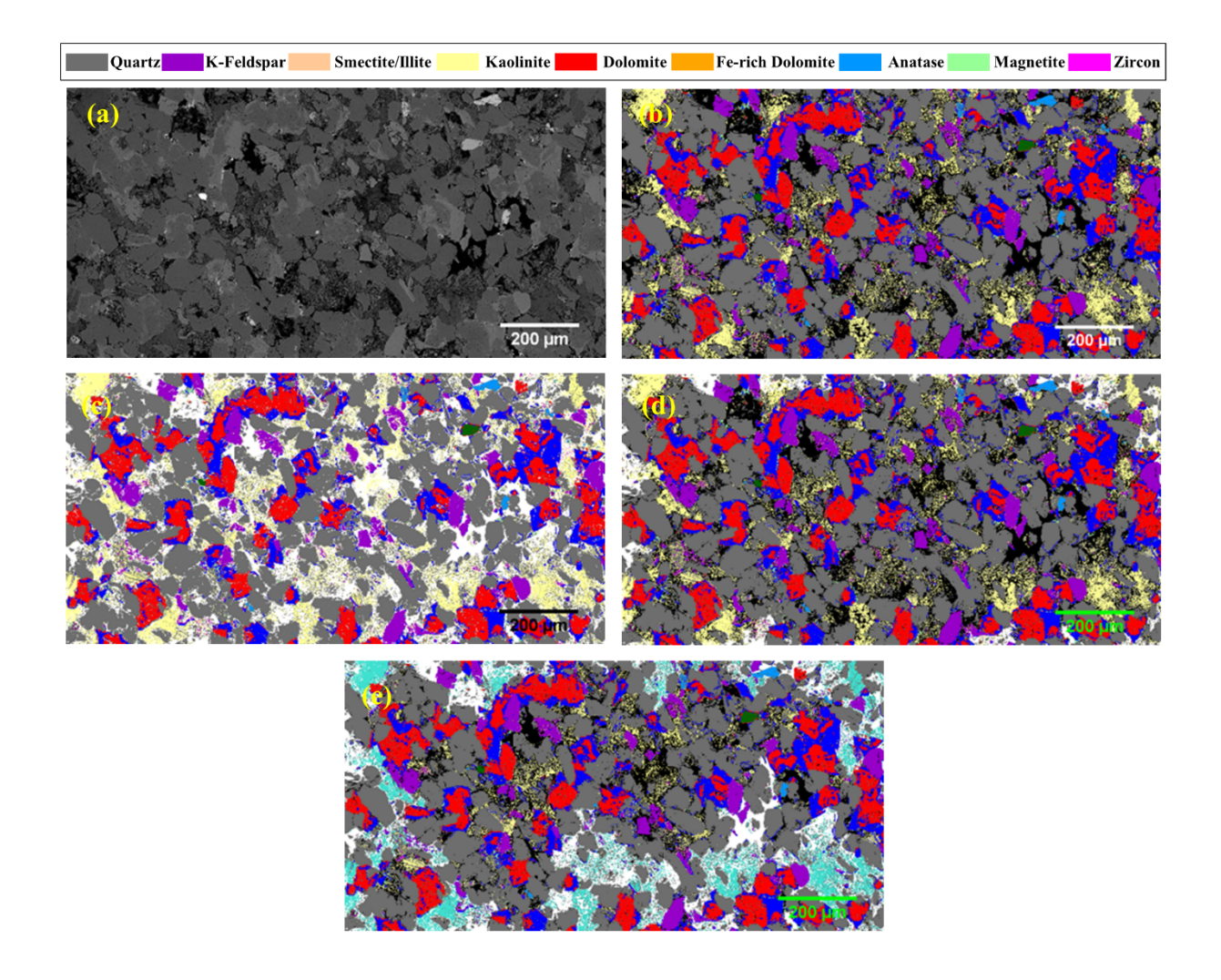


Figure 5: a) SEM BSE image of sample collected from Torrey Buff formation; b) mineral phase segmented map; c) mineral map considering all macropores accessible; d) mineral map considering macropore connectivity; e) mineral map including nanopore connectivity

3.1.6 Lower Tuscaloosa

The SEM BSE image and mineral segmented map of the Lower Tuscaloosa sample are shown in Figures 6a and 6b. Six different minerals are identified, among which quartz is the most dominant phase. Similar to the Bentheimer sample, the sample has a high porosity, about 33% measured from 2D mineral maps. The three types of accessibility maps are shown in Figures 6c, 6d, and 6e. In case of the first approach, the accessibility of quartz is 79.32%, lower than the quartz

abundance. Albite and dolomite accessibility agree well with their abundances. K-feldspar and kaolinite accessibilities are higher, where kaolinite accessibility is about 3.5 times higher than the abundance.

Considering macropore connectivity reduces the effective porosity to 24% (Figure 6d). The accessibility of quartz, in this case about 83%, which is less than its abundance (Figure 6d). Conversely, the accessibility of kaolinite, the major clay mineral, is 13.41%, significantly higher than its abundance. Taking nanopore connectivity into account makes more areas accessible to fluid (shown in red in Figure 1e) and increases the accessibilities of K-feldspar and dolomite. The effective porosity also increases.

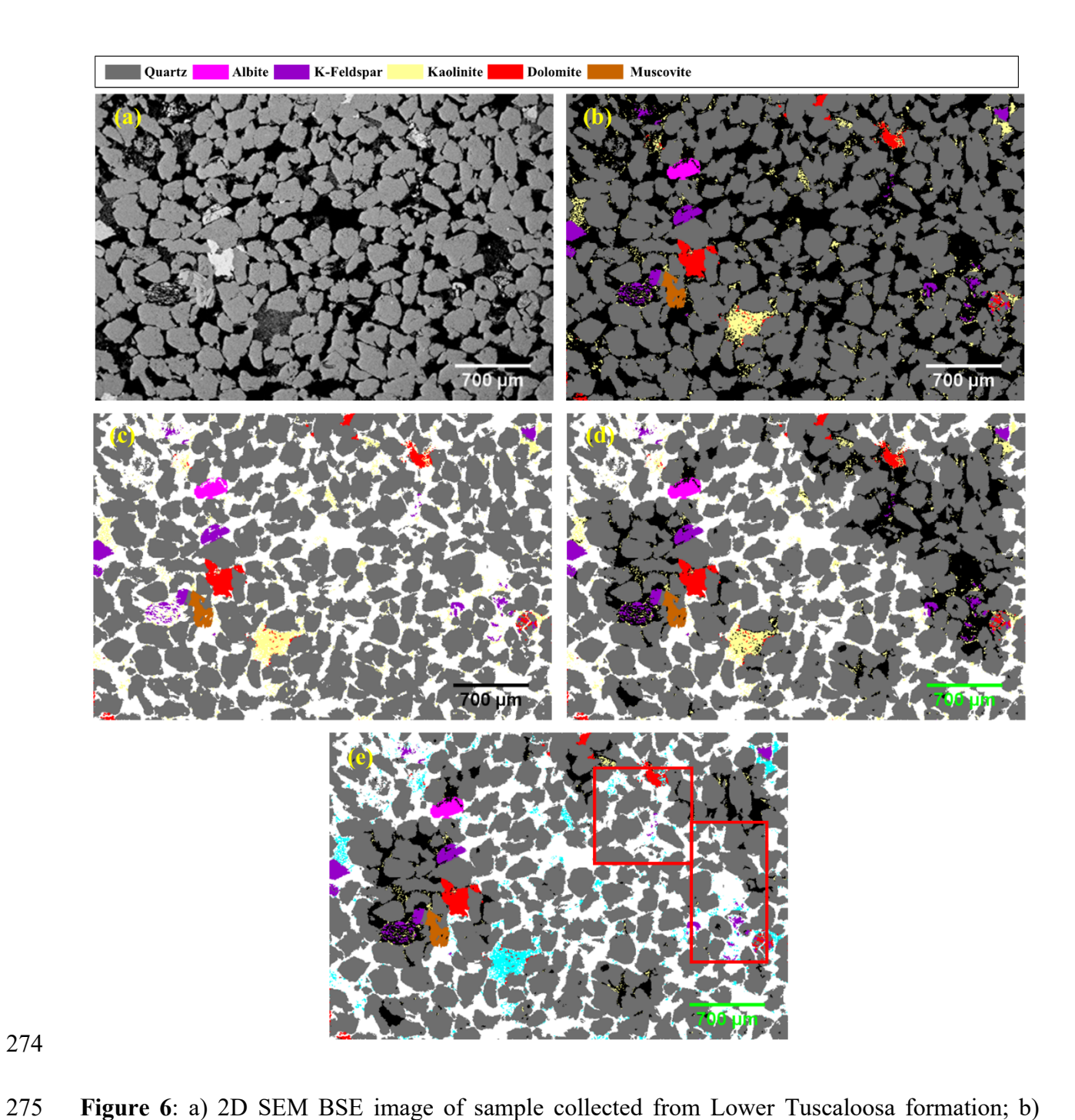


Figure 6: a) 2D SEM BSE image of sample collected from Lower Tuscaloosa formation; b) mineral phase segmented map; c) mineral map considering all macro pore accessible; d) mineral map considering macropore connectivity; e) mineral map including nano pore connectivity

3.1.7 Paluxy

The original and processed images from the Paluxy sandstone are shown in Figures 7 (a and b). Nine minerals are identified in the BSE image, major phases include quartz and albite. The porosity calculated from the BSE image is 19%. When accessibility is determined using the first approach, quartz has lower accessibility than abundance. K-feldspar, albite, calcite, siderite, and muscovite accessibility is slightly larger than their abundances. The two clays, kaolinite and illite have significantly higher accessibilities (16.9% and 2.04%) than their abundances.

Figure 7d presents the mineral map with the macropore connectivity shown in white. In this case, quartz has the highest accessibility, followed by albite and kaolinite. The accessibility of kaolinite is significantly higher than reflected by the abundance of kaolinite. Accessibility values increase for kaolinite, calcite, and illite while they decrease for quartz and albite when nanopore connectivity is considered. Effective porosity determined from macropore and nanopore connectivity approaches are 4.12% and 5.36% respectively, significantly lower than the actual porosity (18.77%).

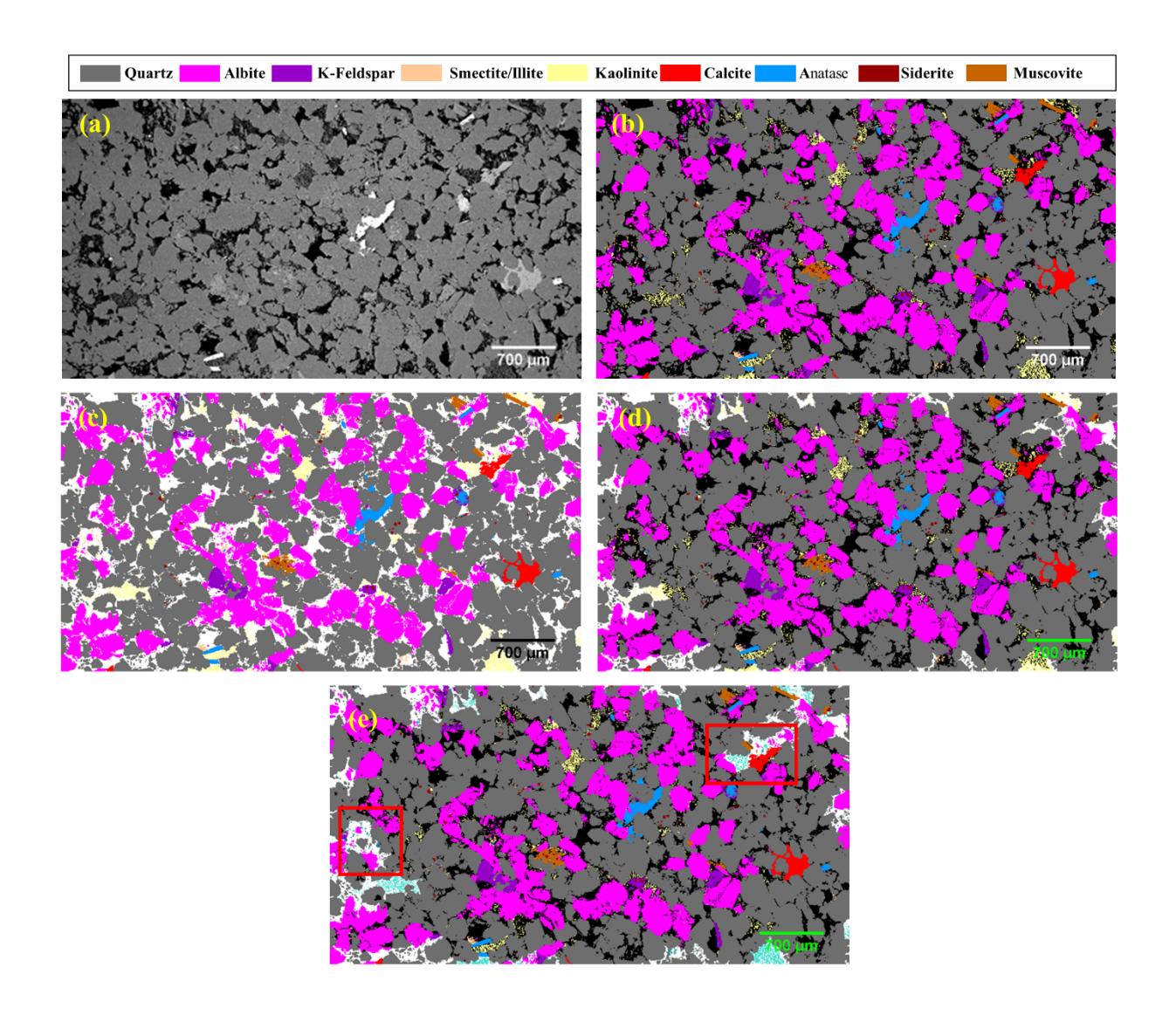


Figure 7: a) SEM BSE image of Paluxy sandstone; b) mineral phase segmented map; c) mineral map considering all macropores accessible; d) mineral map considering macropore connectivity; e) mineral map including nanopore connectivity

3.2 Porosity Comparison

In Figure 8, total porosity and effective porosity are compared for all the samples. Approximately a two to nine times reduction in effective porosity is observed when connectivity is taken into account. The largest drop is evident in the Bandera Gray sample, which has a lower total porosity (15.31%). Consideration of nanopore connectivity increases the effective porosity in

all cases compared to macropore connectivity alone, which is obvious as it reveals more areas for fluid flow. In Figure 8, the Kentucky and Torrey Buff samples have the highest difference between effectivity porosities when nanopores are included, approximately 2.4 times increase. These samples are higher in clay content as compared to the other samples. This is followed by the Bandera Brown sample where effective porosity increases 70% when nanopores are included. The increase in effective porosity include nanopore connectivity for the other samples were all less than a 35% increase.

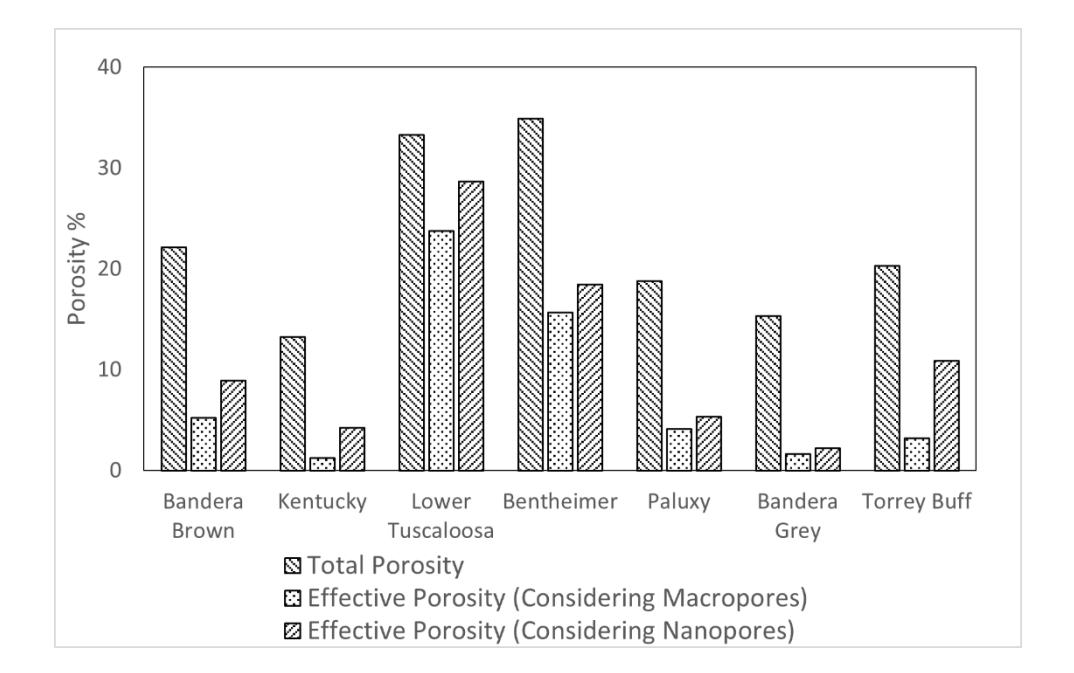


Figure 8: Total porosity and effective porosity comparison for the sandstone samples

3.3 Accessibility Ratio

With the obtained accessibility values from the segmented mineral maps, accessibility ratios are calculated for each mineral. It is calculated by dividing mineral accessibility by mineral abundance for each phase as given by,

$$Accessibility\ Ratio = \frac{\textit{Mineral Accessibility determined from 2D mineral map \%}}{\textit{Mineral Abundance calculated from 2D mineral map \%}}$$

and reported as a unitless number. These ratios provide a normalized reflection of mineral accessibility regardless of mineral quantity for easier comparison among different samples. The value of the ratio being one means that the mineral has the same accessibility as abundance. Accessibility ratios are calculated for quartz, K-feldspar, albite, carbonate, and clay minerals for the three approaches discussed in Section 2.2. If a sample has multiple carbonates or clay minerals, those were combined to reflect total carbonate or clay minerals under a single label for simplicity. Figure 9 shows the accessibility ratio data for all seven samples. For quartz, the accessibility ratios range from 0.53 to 1.12 for all samples and approaches. For all samples except the Kentucky and Paluxy sample, the range is narrower, 0.75 to 1.12. This indicates that accessibility is relatively well reflected by abundance. For the Kentucky and Paluxy samples, the abundance may not reflect the proportion of quartz that will be available for reaction. Consideration of pore connectivity, both macro, and nanopore, has little effect on accessibility for the Lower Tuscaloosa, Paluxy, and Torrey Buff samples. However, for the Kentucky, Bentheimer, Bandera Brown, and Bandera Gray samples, the accessibility ratios change 22-29% with different connectivity approaches. For most samples, the accessibility ratio increases when macropore connectivity is considered; however, for Kentucky, the ratio decreases by 30% (Figure 9). This sample has the lowest porosity among all samples and also low pore connectivity (Figure 4d). Larger variations in accessibility ratio are evident between samples and connectivity approaches for K-feldspar. For the Lower Tuscaloosa, Bentheimer, and Paluxy sample, considering all pores connected results in accessibility ratios above 1, which means that the accessibility is higher than the calculated abundance. The assumption of only macropore connectivity significantly impacts calculated accessibility values, reflected by the change in accessibility ratio of 16-87% with the

317

318

319

320

321

322

323

324

325

326

327

328

329

330

331

332

333

334

335

336

337

highest change (87%) occurring for the Kentucky sample. Considering nanopore connectivity increases the accessibility ratio for all samples (0.9-17%) except for the Bandera Gray.

Albite was identified only in five out of seven samples. If all the macropores are considered, the accessibility ratio varies from 0.54 to 1.18. When the connected macropores are accounted for, the largest variation in computed accessibility is for the Lower Tuscaloosa sample (decreases 32%). When macropore and nanopore connectivity is considered, accessibility ratios typically decrease from values considering only connected macropores. The accessibility ratio for the Bandera Brown sample, however, increases by 43% in this case.

Carbonates are present in all samples except the Kentucky sandstone. The two carbonates identified in the samples are calcite and dolomite, which are very common in sandstone samples. The Bentheimer and Bandera Brown samples have very small amounts of carbonates, 0.0003%, and 0.007%, respectively. As a result, when connectivity is considered, the accessibility is zero for these two samples. Torrey Buff has the highest amount of carbonate minerals (25.32% dolomite) but low accessibility, 6.49%, 2.91%, and 2.65% considering all pores, connected macropores, and connected nanopores, respectively. The resulting accessibility ratios are small. Small values are also evident for the Bandera Gray sample where the accessibility is about five times smaller than the abundance. This represents either coating of carbonate grains with clays or carbonates surrounded by other minerals which makes those grains inaccessible to reactive fluids. Conversely, some samples have accessibility ratios greater than one, indicating more of the carbonate minerals are accessible to reactive fluids than reflected by their abundance. Connectivity does largely impact accessibility ratios for some samples. For the Paluxy sample, a seven times increase in accessibility occurs when nanopore connectivity is taken into account.

Clay minerals are presented in all samples to varying extents (2.5% to 11.7%). This includes kaolinite, smectite/illite, and chlorite. For clay minerals, the accessibility ratio ranges from 2.66 to as high as 16.26. This is due to clay's characteristic occurrence as grain coatings. When nanopore connectivity is included, an increase in accessibility ratio occurs for all of the samples except the Kentucky sandstone. Comparing the accessibility ratios determined by the three approaches, small variations occur for the Bandera Brown, Kentucky, lower Tuscaloosa, Bandera Gray, and Torrey Buff samples, whereas there are large variations in accessibility ratio with the connectivity approach for Bentheimer and Paluxy samples.

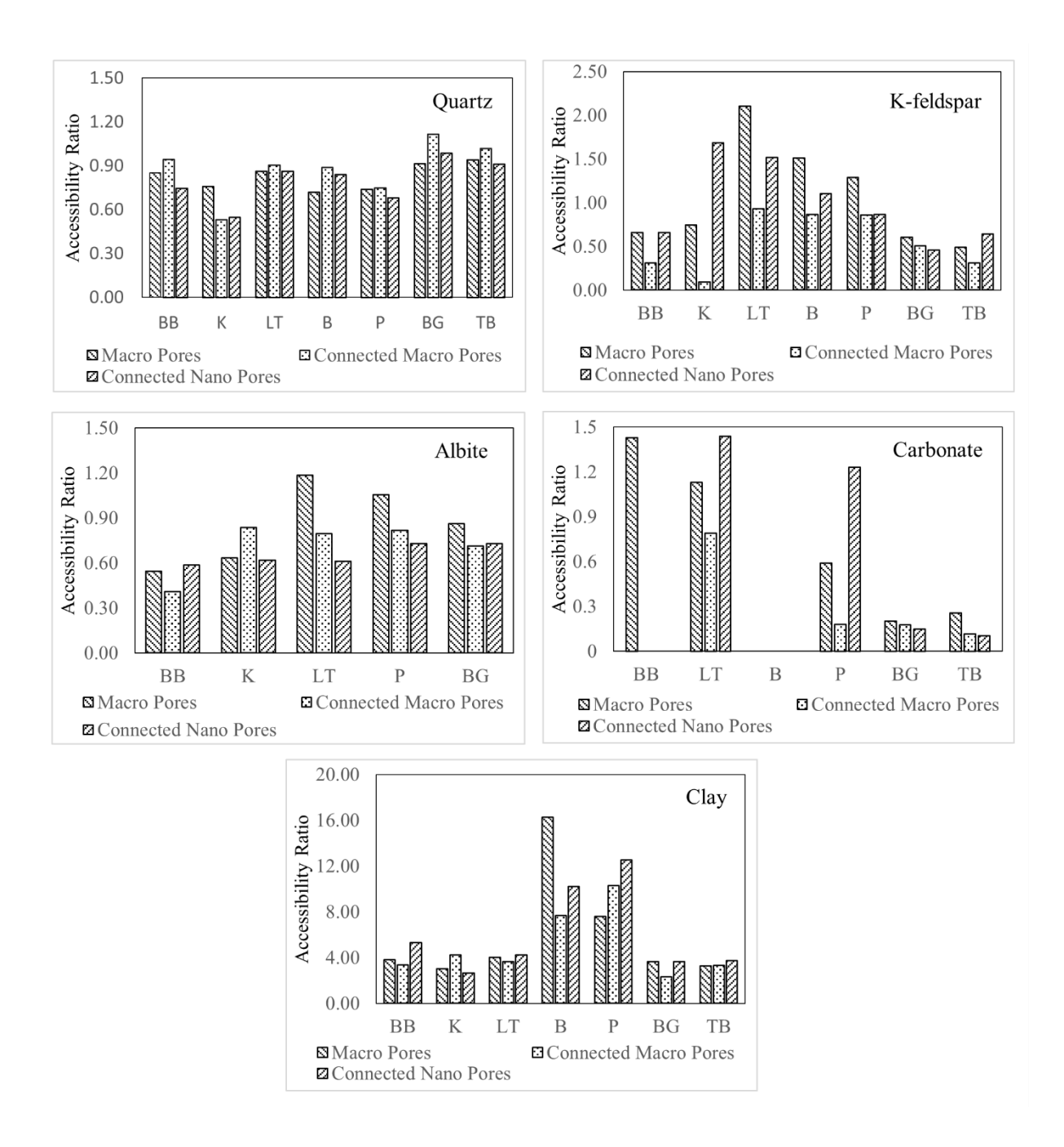


Figure 9: Accessibility ratio comparison for Quartz, K-feldspar, Albite, Carbonate, Clay for all samples

4. Discussion

In this study, we demonstrate the effect of macropore and nanopore connectivity considerations on calculations of mineral accessibility from 2D images. Mineral accessibility was determined using three approaches for seven sandstone samples. Using 2D SEM BSE image in combination with EDS elementals maps, mineral segmented maps were created for these samples. Accessibility values for quartz, K-feldspar, albite, carbonate, and clay minerals were normalized using their abundances to analyze the differences among the three approaches.

The lowest variations in accessibility ratio were noted for quartz with accessibility ratios ranging from 0.53 to 1.12. Larger variations in accessibility ratios were observed for K-feldspar, albite, and carbonate minerals, ranging from 0.09 to 1.5. This indicates the availability of these phases for reaction may be over (ratios less than 1) or under (ratios greater than one) estimated by their volume fractions. Clay minerals have a large range of accessibility ratios, 2.31 to 16.26, indicating their accessibilities tend to be much higher than their abundance, as was similarly observed in prior literature^{22, 24-26}.

Accessibility is also seen to be impacted by the clay content. When clay minerals are present, they often exist as clay coatings on the major mineral phase's surfaces. As a result, the accessibility ratios for other phases will be lower. For example, the accessibility ratio for quartz in the Kentucky sample, which had the highest clay content, was the lowest among all samples considered.

Large variations in accessibility occurred for some mineral phases when nanopore connectivity was considered. Increases in accessibility as high as 17 times estimates considering only macropore connectivity were observed for K-feldspar in the Kentucky sample when nanopore connectivity was taken into consideration. Interestingly, these large variations were not reflected in other mineral phases in the sample where the accessibility of quartz, for example, had little variation when connected macropores and connected nanopores were considered. Large variations in effective porosity are also evident for different approaches to considering pore connectivity. These variations, however, are not always reflected by variations in mineral accessibility. The

effective porosity of the Bandera Gray sample is significantly reduced when considering pore connectivity but little variation in calculated mineral accessibilities occurs.

In terms of predicting reactivity, it is most critical to understand the accessibility of carbonate phases as they often have the fastest reaction rates, e.g. in geologic CO₂ sequestration systems. The accessibility ratios for carbonates in the Bandera Gray and Torry Buff samples are less than 0.3, reflecting low accessibility as compared to abundance. These samples have the highest fraction of carbonate phases, 5.69%, and 25.32%, respectively. As carbonate phases tend to exist as cement between mineral phases, it is anticipated they will have an accessibility ratio of less than one. Higher accessibilities of carbonate phases are observed in the other samples, but these samples all have low fractions of carbonate minerals <1.5% such that it is challenging to make conclusive ties to the accessibility of these phases.

5. Conclusion

In this work, we enhance understanding of mineral accessibility in sandstone samples, to improve understanding of the physical properties of porous materials and ultimately improve modeling reactive transport simulations by better characterizing sample reactivity. Mineral accessibility reflects the availability of minerals for reaction with reactive fluids as is often not considered in reactive transport simulations but may help explain discrepancies with observed field scale reaction rates.

Accuracy of reactive transport modeling, for simulating geologic storage of CO₂ or other applications as discussed in the introduction, largely depends on the precise determination of mineral reaction rates. Excluding the consideration of pore connectivity may provide imprecise estimates of reactivity, mineral reactive surface areas, and thus simulated mineral reaction rates which are directly proportional to reactive surface area. Reactivity may be reduced if grains

surfaces are concealed by clay minerals or inaccessible due to presence as a grain inclusion²⁴. The nanoscale connectivity through thin channels of clay minerals in sandstone samples should also be taken into consideration as it may impacts estimates of surface area of certain minerals covered with those clays^{22,26}. This was observed in recent work which noted reaction rates in flow-through dissolution experiments were effectively simulated accounting for accessibility via connected nano and macropores and rates over estimated assuming all mineral phases were accessible²².

The mineral abundances and accessibilities determined using three approaches for seven sandstone samples reveal the discrepancy between abundance and accessibility. To explore the variation in accessibilities of a particular mineral in different samples, associated accessibility ratios were calculated. As shown in Figure 9, accessibility ratios for K-feldspar, albite and carbonate range within 1.5, while clay minerals have a larger range which agrees well with Peters (2009)²⁴. While useful for comparing the impact of these three approaches, these ratios also have utility for adjusting mineral reactive surface areas in reactive transport simulations to account for variations in accessibility. For example, an accessible mineral surface area could be obtained by multiplying the specific surface area of a given mineral phase (often obtained from the Brunner-Emmett-Teller (BET) method) by the accessibility ratio.

Recent reactive transport modeling work considered implications of variations in surface area on simulated mineral reaction rates and noted little variation in simulation results when surface areas varied within one order of magnitude, as resulting from accessible surface areas determined from images with different resolution^{25,31}. As such, some of the variations in accessibility (within one order of magnitude) observed here for different pore connectivity approaches are not anticipated to largely impact simulated mineral reactions or reaction rates. Observed variations in accessibility for clay and carbonate minerals, however, may be important. Due to its fast reaction

rate, differences in carbonate mineral accessibility are only anticipated to impact simulation reactions on short time scales (hours to days) where even large differences in calcite surface area values were insufficient in terms of the overall simulation results at long time scales (years) in Qin and Beckingham (2021)³¹. Clay mineral accessibility determined here varies up to one order of magnitude so larger impacts in simulated associated reaction rates may occur. Due to the slower reaction rate of these phases, this is anticipated to impact only longer simulated time scales (years) but will likely not be significant for simulations interested in short time scales (hours to days)³¹.

6. Acknowledgements

- This material is based upon work supported by the National Science Foundation under Grant
- 453 No: 1847243.

444

445

446

447

448

449

450

- 454 Supporting Information Available
- SEM BSE image properties of each sample
- Mineral accessibility determined using the three approaches for all samples
- 457 References
- 458 1. Brantley, S. L., Holleran, M. E., Jin, L. & Bazilevskaya, E. Probing deep weathering in the
- Shale Hills Critical Zone Observatory, Pennsylvania (USA): The hypothesis of nested
- chemical reaction fronts in the subsurface. Earth Surf. Process. Landforms (2013).
- 461 doi:10.1002/esp.3415
- 462 2. Parry, S. A., Hodson, M. E., Kemp, S. J. & Oelkers, E. H. The surface area and reactivity
- of granitic soils: I. Dissolution rates of primary minerals as a function of depth and age
- deduced from field observations. *Geoderma* (2015). doi:10.1016/j.geoderma.2014.08.004

- 465 3. Maher, K., Steefel, C. I., White, A. F. & Stonestrom, D. A. The role of reaction affinity and
- secondary minerals in regulating chemical weathering rates at the Santa Cruz Soil
- 467 Chronosequence, California. Geochim. Cosmochim. Acta (2009).
- 468 doi:10.1016/j.gca.2009.01.030
- 469 4. Goh, K. H. & Lim, T. T. Geochemistry of inorganic arsenic and selenium in a tropical soil:
- Effect of reaction time, pH, and competitive anions on arsenic and selenium adsorption.
- 471 *Chemosphere* (2004). doi:10.1016/j.chemosphere.2003.11.041
- 5. Sandhu, D. *et al.* Fate and transport of radioactive gypsum stack water entering the Floridan
- 473 aquifer due to a sinkhole collapse. Sci. Rep. (2018). doi:10.1038/s41598-018-29541-0
- 474 6. Essaid, H. I., Bekins, B. A. & Cozzarelli, I. M. Organic contaminant transport and fate in
- the subsurface: Evolution of knowledge and understanding. *Water Resour. Res.* (2015).
- 476 doi:10.1002/2015WR017121
- 7. Crandell, L. E., Peters, C. A., Um, W., Jones, K. W. & Lindquist, W. B. Changes in the pore
- 478 network structure of Hanford sediment after reaction with caustic tank wastes. *J. Contam.*
- 479 *Hydrol.* (2012). doi:10.1016/j.jconhyd.2012.02.002
- 480 8. Deng, Y., Harsh, J. B., Flury, M., Young, J. S. & Boyle, J. S. Mineral formation during
- simulated leaks of Hanford waste tanks. Appl. Geochemistry (2006).
- 482 doi:10.1016/j.apgeochem.2006.05.002
- 483 9. Xiao, Y., Xu, T. & Pruess, K. The effects of gas-fluid-rock interactions on CO2 injection
- and storage: insights from reactive transport modeling. *Energy Procedia* 1, 1783–1790
- 485 (2009).
- 486 10. Tang, Y. et al. Experiment on CO2-brine-rock interaction during CO2 injection and storage

- in gas reservoirs with aquifer. *Chem. Eng. J.* **413**, 127567 (2021).
- 488 11. Abedini, A. & Torabi, F. On the CO2 storage potential of cyclic CO2 injection process for
- enhanced oil recovery. *Fuel* **124**, 14–27 (2014).
- 490 12. Jessen, K., Kovscek, A. R. & Orr Jr, F. M. Increasing CO2 storage in oil recovery. *Energy*
- 491 *Convers. Manag.* **46**, 293–311 (2005).
- 492 13. Emberley, S. et al. Geochemical monitoring of fluid-rock interaction and CO2 storage at
- the Weyburn CO2-injection enhanced oil recovery site, Saskatchewan, Canada. *Energy* **29**,
- 494 1393–1401 (2004).
- 495 14. Dai, Z. et al. Uncertainty quantification for CO2 sequestration and enhanced oil recovery.
- 496 Energy Procedia **63**, 7685–7693 (2014).
- 497 15. Bachu, S. Sequestration of CO2 in geological media: Criteria and approach for site selection
- in response to climate change. *Energy Convers. Manag.* **41**, 953–970 (2000).
- 499 16. Iloejesi, C. O. & Beckingham, L. E. Assessment of geochemical limitations to utilizing CO2
- as a cushion gas in compressed energy storage systems. *Environ. Eng. Sci.* **38**, 115–126
- 501 (2021).
- 502 17. White, A. F. & Peterson, M. L. Role of reactive-surface-area characterization in
- geochemical kinetic models. in (ACS Publications, 1990).
- White, A. F. & Brantley, S. L. The effect of time on the weathering of silicate minerals:
- why do weathering rates differ in the laboratory and field? Chem. Geol. 202, 479–506
- 506 (2003).
- 507 19. Navarre-Sitchler, A. & Brantley, S. Basalt weathering across scales. *Earth Planet. Sci. Lett.*
- **261**, 321–334 (2007).

- 509 20. Lüttge, A., Arvidson, R. S. & Fischer, C. A stochastic treatment of crystal dissolution
- 510 kinetics. *Elements* **9**, 183–188 (2013).
- 511 21. Bourg, I. C., Beckingham, L. E. & DePaolo, D. J. The nanoscale basis of CO2 trapping for
- 512 geologic storage. *Environ. Sci. Technol.* **49**, 10265–10284 (2015).
- 513 22. Beckingham, L. E. et al. Evaluation of accessible mineral surface areas for improved
- prediction of mineral reaction rates in porous media. *Geochim. Cosmochim. Acta* (2017).
- 515 doi:10.1016/j.gca.2017.02.006
- 516 23. Noiriel, C. & Daval, D. Pore-scale geochemical reactivity associated with CO2 storage: new
- frontiers at the fluid–solid interface. Acc. Chem. Res. 50, 759–768 (2017).
- 518 24. Peters, C. A. Accessibilities of reactive minerals in consolidated sedimentary rock: An
- imaging study of three sandstones. *Chem. Geol.* **265**, 198–208 (2009).
- 520 25. Qin, F. & Beckingham, L. E. Impact of image resolution on quantification of mineral
- abundances and accessible surface areas. *Chem. Geol.* **523**, 31–41 (2019).
- 522 26. Landrot, G., Ajo-Franklin, J. B., Yang, L., Cabrini, S. & Steefel, C. I. Measurement of
- accessible reactive surface area in a sandstone, with application to CO 2 mineralization.
- 524 Chem. Geol. **318–319**, 113–125 (2012).
- 525 27. Ma, J., Ahkami, M., Saar, M. O. & Kong, X.-Z. Quantification of mineral accessible surface
- area and flow-dependent fluid-mineral reactivity at the pore scale. *Chem. Geol.* **563**, 120042
- 527 (2021).
- 528 28. Soong, Y. et al. CO2/brine/rock interactions in Lower Tuscaloosa formation. Greenh. Gases
- 529 Sci. Technol. 6, 824–837 (2016).
- 530 29. Guan, S. Modeling geomechanical property changes using well logging and pressure data

531 in a carbon dioxide enhanced oil recovery reservoir. ProQuest Dissertations and Theses 532 (Colorado School of Mines, 2012). Beckingham, L. E. et al. Evaluation of mineral reactive surface area estimates for prediction 533 30. of reactivity of a multi-mineral sediment. Geochim. Cosmochim. Acta 188, 310-329 (2016). 534 Qin, F. & Beckingham, L. E. The impact of mineral reactive surface area variation on 535 31. 536 simulated mineral reactions and reaction rates. Appl. Geochemistry 124, 104852 (2021). 537 538